J Mater Sci (2010) 45:448–459
DOI 10.1007/s10853-009-3961-2

Analysis of the essential work of fracture method as applied to UHMWPE

S. Naz · J. Sweeney · P. D. Coates

Received: 6 July 2009 / Accepted: 5 October 2009 / Published online: 21 October 2009

Abstract The validity of the basic assumptions behind the method of essential work of fracture (EWF), as applied to ultra-high molecular weight polyethylene (UHMWPE), is evaluated using finite element modelling. To define a suitable model of constitutive behaviour, the mechanical properties of UHMWPE have been measured in both uniaxial tension and compression over a range of strain rates. The observed strain rate dependence of stress, including the observed differences in strain rate sensitivity between tension and compression, is interpreted in terms of a single Eyring process. The constitutive theory is constructed comprising an Eyring process and hyperelastic networks, the latter having responses symmetric with respect to tension and compression. This theory is implemented within a finite element scheme, and used to model fracture measurements made on the same material using double-edge notch tensile specimens. Calculations of the non-essential work and of the extent of the plastic zones are thus made possible. It is concluded that the specific non-essential work is essentially constant, but that the shape factor β, assumed constant in the conventional analysis, varies significantly with ligament length. The implication of this finding on the derived EWF value is evaluated and found to be slight.

S. Naz · J. Sweeney (✉) · P. D. Coates
School of Engineering, Design and Technology/IRC in Polymer Science and Technology, University of Bradford, Bradford BD7 1DP, UK
e-mail: j.sweeney@bradford.ac.uk

Present Address:
S. Naz
Ford Motor Company, Dagenham Diesel Centre, Kent Avenue, Dagenham RM9 6SA, UK

Introduction

Ultra-high molecular weight polyethylene (UHMWPE) is of key importance in structural applications in the medical implant field, where it is subject to complex stress fields and wear at bearing surfaces. We require a detailed understanding of its mechanical behaviour if we are to predict its behaviour in these circumstances, as is necessary when, for instance, finite element modelling is to be used. As with all polymers, UHMWPE becomes nonlinear at moderate strains and exhibits creep, stress relaxation and strain-rate dependent yielding. Because of its low yield stress, fracture phenomena are accompanied by large plastic zones, leading to complications in both fracture testing and analysis. In this paper we address both these issues. We have investigated the mechanical behaviour of UHMWPE and introduced a constitutive model that reflects the observed complex behaviour, while remaining tractable for application in engineering analyses. We have also measured fracture behaviour using experiments in the post-yield regime. Finally, we have implemented our constitutive model in a finite element program and used the resulting analysis to simulate the fracture experiments. Here we have addressed two basic issues: the constancy of the non-essential work; and the constancy of the plastic zone shape factor.

Our constitutive model is constructed by combining Eyring processes and hyperelastic network models. The Eyring process results in an appropriate form of the dependence of stress on time and rate of strain, so that rate-dependent yield and viscoelastic phenomena such as non-linear creep and stress relaxation are encompassed by the model. A programme of tensile and compressive uniaxial experiments over a range of strain rates is used to establish the Eyring parameters. The use of an Eyring process that

includes both pressure and shear terms enables the modelling of the somewhat different strain rate dependences of stress that are observed between tensile and compressive behaviour. To enable the model to cover moderately large deformations, we have introduced hyperelastic networks. The form of network is chosen so as to accommodate the observed stress–strain behaviour that, over the strain range covered, is approximately symmetric between tension and compression. The primary aim of the model is to provide an adequate representation of the material behaviour in the fracture specimens.

In a series of papers, Bergström et al. [1–3] have developed constitutive models for UHMWPE. They have combined hyperelastic and rate dependent plastic elements to produce models of both conventional and highly cross-linked UHMWPE. Rather than using an Eyring model of plasticity, in their 'hybrid model' they use a power law that does not include a pressure term. Most significantly, they explore higher strains than covered here, going outside the range for which the tensile and compressive responses are approximately equal. Our relatively simple model operates sufficiently well within the strain range required for modelling the fracture experiments.

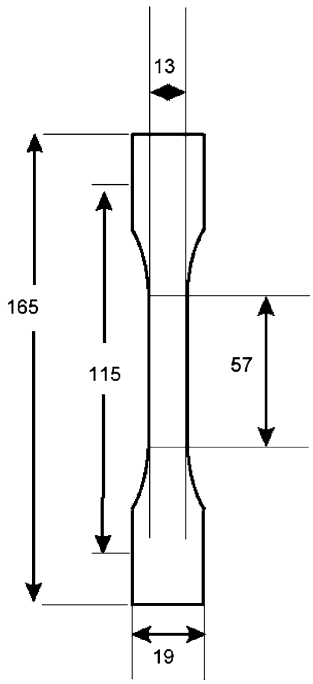

Fig. 1 Tensile specimen geometry. Dimensions in mm. The 115 mm distance is the grip separation

Material and experimentation

In all tests UHMWPE grade GUR1050 was used, manufactured by Hoechst and supplied by Orthoplastics, Todmorden Road, Bacup, Lancs, UK in the form of compression moulded blocks. The molar mass of this grade of polymer has been estimated in the range 5.5–6.0 $\times$ 10^6 g mol^{-1} using intrinsic viscosity measurements [4]. The crystallinity of the sample was determined at a value of 40.96% as quantified using modulated differential scanning calorimetry performed on a TA Instruments Q2000 DSC imposing a $\pm$0.5 °C oscillation every 40 s onto a mean temperature ramp of 5 °C/min. The area under the non-reversing heat capacity curve was divided by the heat of fusion for a 100% crystalline sample, taken as 293 J/g.

Uniaxial tests were carried out in both tensile and compressive modes using an Instron testing machine model 5568 operating at room temperature. The tensile specimen geometry shown in Fig. 1 is based on a type I ASTM D638 standard. For the tensile tests, strains were measured with the aid of a video extensometer (MessPhysik ME46NG) that sensed the separation of two parallel pen lines 50 mm apart on the 105 mm parallel gauge length. Tests were carried out at constant speeds, which resulted in approximately constant rates of engineering strain in the range 0.005–0.08 s^{-1}. These and other quoted experimental rates of strain refer to the initial strain rate, i.e. at the start of the test. For the compressive tests, specimens were in the form of circular cylinders of diameter and height 10 mm, with faces machined to an average surface roughness of 5–6 μm. Specimens were compressed at constant speed between steel platens, with strains derived with good accuracy using the machine displacement, as verified by checking with a dial gauge extensometer. Engineering strain rates were in the range 0.001–0.017 s^{-1}. Specimens were strained to a final extension ratio of 0.67, corresponding to a true strain of -0.4. Photographs of the specimens taken immediately after testing showed no signs of barrelling in this range of strain rates, indicating truly uniaxial conditions and no significant friction effects.

Fracture measurements were carried out using the essential work of fracture (EWF) method. The EWF method was developed as an alternative to the J-Integral method in order to evaluate the fracture toughness of ductile materials. It is considered to be less time consuming and simpler to use [5, 6] and has been implemented by various researchers [7–10] since it was first proposed by Broberg [11]. Mai et al. [12] have applied the method to UHMWPE. Double edge notch tensile specimens were used with geometries as illustrated in Fig. 2, with ligament lengths varying from 2 to 11 mm. The specimen thickness was either 1.5 or 3 mm, in either case ensuring plane stress conditions. The edge notches were in the form of machined slits, sharpened to a further depth of 0.5 mm using a razor blade driven via an attachment by the Instron tester. The fracture tests were accomplished using the Instron testing

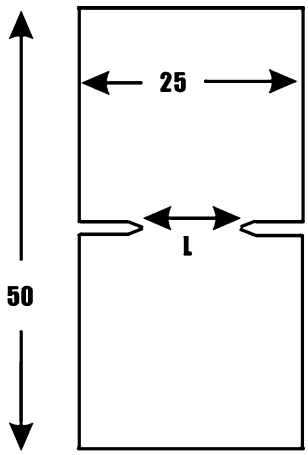

Fig. 2 Fracture specimen geometry. Dimensions in mm

machine operating at room temperature at a testing speed 10 mm/min. Video images of the specimens, including the ligament lengths and both crack tips, were captured at a rate of 10 frames/s using a Pixelink model PL-741 digital video camera, enabling observation of the ligament and the crack tips during testing.

Fundamentals of constitutive behaviour

Stress–strain curves for the rate 0.01 s^{-1} are shown in Fig. 3, where compressive and tensile behaviours are compared. Here, as elsewhere, true stresses are plotted as calculated on the assumption of incompressibility. The shapes of the curves are similar for all rates. The difference between the tensile and compressive result remains small, provided true (logarithmic) strain is plotted, as found previously in this strain range [2].

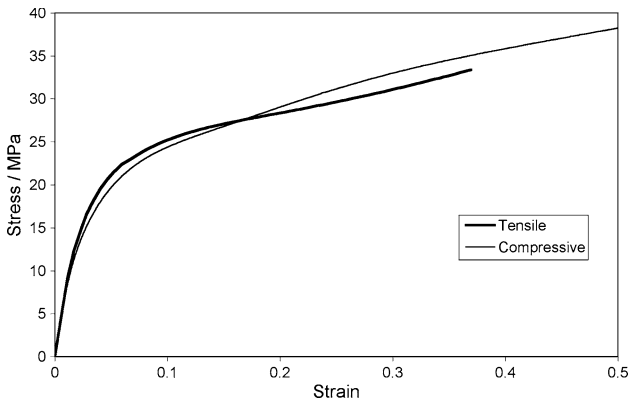

Fig. 3 Tensile and compressive stress–strain curves at strain rate 0.01 s^{-1}

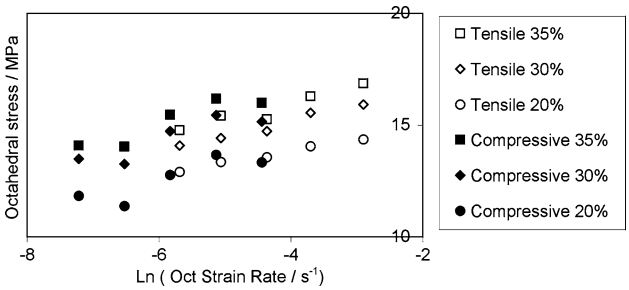

Fig. 4 Strain rate dependence of stress

Strain rate dependence of stress is plotted in Fig. 4. We observe that the stress is an essentially linear function of the logarithm of the initial strain rate. This applies in both tension and compression. It is well known [13–15] the strength of the strain rate dependence of stress—the strain rate sensitivity—is a crucial influence in the growth of instabilities in the form of strain localisation such as necking, and so is crucially important for accurate strain predictions.

The observed rate dependence can be modelled well using an Eyring process, as is well-established [16]. For such a process, the scalar plastic strain rate $\dot{e}_p$ is given by

$$\dot{e}_p = A \exp(V_p \bar{\boldsymbol{\sigma}}) \sinh(V_s \boldsymbol{\tau}), \tag{1}$$

where $\dot{e}_p$ is the octahedral strain rate, defined in terms of the plastic strain rate tensor $\mathbf{D}^p$ by:

$$\dot{e}_p = \sqrt{\frac{1}{3}\mathbf{D}^p : \mathbf{D}^p}. \tag{2}$$

The parameters A, V_p and V_s are temperature-dependent material constants, the latter two being proportional to pressure and shear activation volumes, respectively. $\bar{\boldsymbol{\sigma}}$ is the mean stress and τ is the octahedral shear stress. For a Cauchy stress tensor $\boldsymbol{\Sigma}$, the mean stress is given by

$$\bar{\boldsymbol{\sigma}} = \frac{1}{3}\mathrm{tr}(\boldsymbol{\Sigma}), \tag{3}$$

the stress deviator tensor $\boldsymbol{\tau}$ by

$$\boldsymbol{\tau} = \boldsymbol{\Sigma} - \bar{\boldsymbol{\sigma}}\mathbf{I}, \tag{4}$$

and the octahedral shear stress by

$$\tau = \sqrt{\frac{1}{3}\boldsymbol{\tau} : \boldsymbol{\tau}}. \tag{5}$$

To complete the formulation, the components of the plastic strain rate tensor are related to the stress deviator by the Lèvy–Mises flow rule:

$$\frac{\mathbf{D}^P}{\dot{e}^p} = \frac{\boldsymbol{\tau}}{\tau}. \tag{6}$$

This supplies components of the symmetric strain rate tensor. The method used to increment the plastic strain

using these components is given below in the section 'FE modelling and analysis'.

In Eq. 1, it is often useful to assume that the hyperbolic sine function has arguments large enough for it to approximated by an exponential. Then, for a uniaxial stress σ, (1) becomes

$$\dot{e}_p = \frac{1}{2}A\exp\left\{\frac{1}{3}V_p\sigma + \frac{\sqrt{2}}{3}V_s|\sigma|\right\}. \tag{7}$$

This is equivalent to

$$\frac{1}{3}V_p\sigma + \frac{\sqrt{2}}{3}V_s|\sigma| = \ln\left(\frac{2\dot{e}_p}{A}\right). \tag{8}$$

When uniaxial stress is plotted against the logarithm of strain rate, the result is thus predicted to be linear, with gradient

$$\begin{cases} \left(-\frac{1}{3}V_p + \frac{\sqrt{2}}{3}V_s\right)^{-1} & \sigma < 0 \\ \left(\frac{1}{3}V_p + \frac{\sqrt{2}}{3}V_s\right)^{-1} & \sigma > 0 \end{cases} \tag{9}$$

The expected difference in gradient in tension and compression has been noted by Chow [17]. We may envisage that a component of a material constitutive model consists of an Eyring process in series with an elastic element. Then, at yield, the applied strain rate is equal to the plastic strain rate. Working on the basis of such a model, if both compressive and tensile data are available as a function of strain rate, it should be possible to identify both V_p and V_s by the use of the above equations.

The stress–strain curves of Fig. 3 show behaviour that can be interpreted as a combination of yielding and continued elastic deformation. We propose a model that can be represented schematically by the diagram in Fig. 5. There are many precedents for this configuration, perhaps the earliest being due to Haward and Thackray [18]. One arm of the model is as described above, comprising an Eyring process in series with an elastic element. Consider that this model is subject to a constant rate of strain. Then, once the Eyring process is completely activated, the stress in this arm becomes constant, as does the strain in the elastic element. The stress in the other purely elastic arm then continues to increase, so that the sum of the stresses in the two arms evolves in a manner similar to that of the stress observed in Fig. 3. From that figure, it appears that the yielding of the Eyring process is complete at a strain of 0.15–0.2, when the slope ceases to decrease. According to the proposed model, after yielding the total stress is equal to the yield stress plus a quantity that depends only upon strain. Then, plotting stress as a function of logarithmic rate at a series of constant strains, as has been done in Fig. 4, should give a series of straight lines with gradients differing only to the small extent that results from different levels of hydrostatic pressure. This is pursued in the next section.

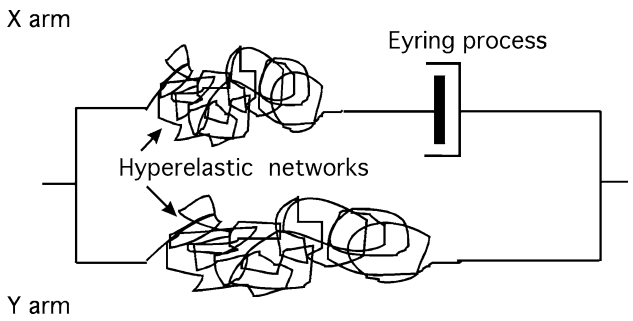

Fig. 5 Schematic of proposed model

To accommodate the large deformations, the elastic elements are assumed to be hyperelastic. At the relatively modest extension ratios that we are to model, finite strain extensibility is not an issue, and so the Gaussian hyperelastic theory presents itself as a possible model. The drawback of this model is that it does not produce a stress response that is symmetric when comparing compressive and tensile strains, as observed to a good approximation in Fig. 3. At the strain rates here (equivalent to $\ln(\dot{e}) = -5$ in Fig. 4), the difference between the stresses in compression and tension from the Eyring mechanism is small, but consistent with that observed in the experiments. The best strategy is to use a network that is symmetric with respect to tension and compression, and to model any observed small asymmetry via the Eyring mechanism. Therefore, we introduce the hyperelastic model defined by strain energy function

$$W = \frac{1}{2}C\left(\lambda_I^2 + \lambda_{II}^2 + \lambda_{III}^2 + \lambda_I^{-2} + \lambda_{II}^{-2} + \lambda_{III}^{-2} - 6\right). \tag{10}$$

Here I, II and III are the principal directions of strain and C is a material constant. For any principal direction i, W is symmetric with respect to interchange of λ_i, and $1/\lambda_i$, or equivalently of the true strains $\ln\lambda_i$ and $-\ln\lambda_i$. This strain energy function is a form of Mooney–Rivlin model. We assume the material to be incompressible, with

$$\lambda_I\lambda_{II}\lambda_{III} = 1. \tag{11}$$

Principal stresses are then given by

$$\sigma_i = \lambda_i\frac{\partial W}{\partial\lambda_i} - p \quad (i = \text{I, II, III}), \tag{12}$$

where p is an unknown hydrostatic pressure. Under the plane stress conditions of interest here with $\sigma_{III} = 0$, p can be eliminated to give

$$\sigma_i = \lambda_i\frac{\partial W}{\partial\lambda_i} - \lambda_{III}\frac{\partial W}{\partial\lambda_{III}}(i = \text{I, II}). \tag{13}$$

There are two such networks included in this constitutive model, one in the X arm and one in the Y arm

parameterised, respectively, by C_X and C_Y. In the X arm, principal stresses are given by

$$\sigma_i = C_X\left(\left(\lambda_i^{eX}\right)^2 - \left(\lambda_i^{eX}\right)^{-2} + \left(\lambda_I^{eX}\lambda_{II}^{eX}\right)^2 - \left(\lambda_I^{eX}\lambda_{II}^{eX}\right)^{-2}\right) \quad (i = \text{I, II}), \tag{14}$$

where the λ_i^{eX} are the principal extension ratios applied to the network. Note that the total principal extension ratios λ_i are related to the elastic and plastic principal extension ratios multiplicatively by

$$\lambda_i = \lambda_i^{eX}\lambda_i^{p} \quad (i = \text{I, II}), \tag{15}$$

where the λ_i^{p} are principal values of the plastic strain tensor $\mathbf{V^p}$.

For the Y arm, principal stresses are given by

$$\ldots\sigma_i = C_Y\left(\lambda_i^2 - \lambda_i^{-2} + (\lambda_I\lambda_{II})^2 - (\lambda_I\lambda_{II})^{-2}\right) \quad (i = \text{I, II})\ldots \tag{16}$$

Material constitutive parameters

When using the above Eyring analysis and examining the stress as a function of strain rate to apply Eq. 8 and expressions (9), it becomes apparent that there is some systematic increase of the gradient with strain, as shown in Fig. 4. This suggests that the model is an over-simplification, and that to include several Eyring processes rather the single one used here would be more realistic. Then, yielding could take place over a range of strains, with processes with lower activation volumes coming into operation at higher strains. However, we shall establish that this model gives a highly useful representation of the material while providing a manageable implementation, and we shall use values of gradient averaged over the measured strain range. Thus, the gradient in tension over all strains is found to be 1.37 ± 0.23 MPa, and for compression the corresponding result is 1.66 ± 0.37 MPa. Here the errors span 95% confidence intervals, and the two gradients are significantly different from each other at the 15% level. We proceed to use the analysis embodied in (8) and (9) to derive values of both V_p and V_s. On this basis, the measured gradients give $V_p = 0.2 \pm 0.04$ and $V_s = 1.5 \pm 0.33$ MPa^{-1}. These parameters are related to the pressure and shear activation volumes v_p and v_s, respectively, by

$$V_p = \frac{v_p}{kT}, \quad V_s = \frac{v_s}{kT}, \tag{17}$$

where k is Boltzmann's constant and T the absolute temperature. Our parameter values derived above correspond to $v_p = 1.3$ nm^3 and $v_s = 7.3$ nm^3, with ratio $v_p/v_s = V_p/V_s = 0.13$.

There are few published values of the ratio v_p/v_s in the literature. In the case of amorphous polymers, Nazarenko et al. [19] have proposed the value of 0.06 for polycarbonate, while Bauwens-Crowet and Bauwens [20] have proposed for the same material the value 0.075, while noting values in the range 0.05–0.072 obtained by other workers. In the case of semicrystalline polymers, Joseph and Duckett [21], using a high pressure measurement technique, derived for polypropylene a room pressure value for the ratio of 0.15. Using similar techniques with polyethylene, and working over a wider range of strain rate than in this study, Truss et al. [22] detected two Eyring processes, with ratios of 0.035 and 0.063.

There are some absolute values of activation volume available for comparison in the literature. The values of Truss et al. [22] were obtained with polyethylene using torsion experiments. When corrected for the use of shear stress rather than octahedral shear stress in their Eyring equation, the shear activation volumes that they derive for their two-process model correspond to 4.5 and 8.0 nm^3, the latter very close to that derived here. Often, experiments in uniaxial tension are used to derive a combined activation volume from the observed strain rate dependence of yield; by inspection of Eq. 7, such a combined activation volume parameter v is given by

$$v = \frac{1}{3}v_p + \frac{\sqrt{2}}{3}v_s. \tag{18}$$

On this basis, our activation volumes correspond to $v = 3.9$ nm^3. This compares with the value obtained in tension for polyethylene of Brooks et al. [23] equivalent (taking into account a factor of 2 in the argument of their sinh term) to $v = 2.42$ nm^3.

The above discussion shows that our values of activation volume are comparable to those derived by other workers. It is to be expected that different polyethylenes will show somewhat different activation volumes on the basis of having different detailed structure. In particular, in the work of Gueguen et al. [24] it is assumed that yielding is a co-operative process involving activation volumes for both the crystalline and amorphous phases. The effective activation volume is then a function of both the crystal and amorphous activation volumes and of the degree of crystallinity. Some of the observed differences in Eyring parameters are then attributable to different levels of crystallinity.

The values of the model parameters use to fit the material behaviour are summarised in Table 1. Resulting predictions of stress–strain curves are compared with observation in Fig. 6 for both tension and compression at strain rates selected to include the extremes covered in tension and compression. Yielding is predicted to take place more abruptly than is observed, as a consequence of

Table 1 Parameters used for the constitutive model

C_X, MPa	C_Y, MPa	A, s^{-1}	V_p, MPa^{-1}	V_s, MPa^{-1}
136	4.0	7.3×10^{-9}	0.19	1.41

the single Eyring process used in the model. A more complex model including a spectrum of processes could represent the yield process more precisely, but at the expense of greater computational complexity.

Fracture analysis and results

Using the EWF method, in which for each tensile test fracture is induced along the whole of the ligament length L, it is assumed that the total work W on the specimen is divided into the essential work W_e required to create the crack surface and the non-essential work W_{ne}, associated with plastic deformation:

$$W = W_e + W_{ne}. \tag{19}$$

For a specimen of thickness t, the total crack area is Lt, and we may introduce specific essential work of fracture u_e:

$$u_e = W_e/Lt. \tag{20}$$

We also introduce the non-essential specific work u_{ne}. However, as this component is associated with the volume of yielded material, it is related to the W_{ne} via the plastic zone volume. This quantity is not readily calculable, but is assumed to be a volume adjacent to the crack surface with average extent βL from the crack. The plastic zone volume is then $\beta L^2 t$ and we may write

$$W_{ne} = u_{ne}\beta L^2 t, \tag{21}$$

where β is known as the shape factor. Dividing Eq. 19 by Lt and using Eqs. 20 and 21 gives

$$u = u_e + u_{ne}\beta L, \tag{22}$$

where $u = W/Lt$. The quantity u can be measured for a range of ligament lengths. The conventional analysis is to assume that β is constant and to extrapolate the resulting linear equation (22) to find $u_e = u$ at $L = 0$. The constancy of β is a questionable assumption and the general validity of Eq. 22 has been questioned, and successfully replaced by a nonlinear expression [25]. This issue will be examined in a later section using finite element modelling. However, in this section we will produce results using the conventional interpretation.

To use the EWF method described above, double-edge notch tensile specimens (Fig. 2) were tested to give results typified in Figs. 7 and 8 as plots of applied remote stress versus specimen extension, for the 1.5 and 3.0 mm thick specimens, respectively. The energies to fracture for both specimen thicknesses are plotted in Fig. 9 to give a single extrapolated value for the EWF u_e at zero ligament length of 66 ± 15 kJ/m^2, according to Eq. 22 under the assumption of a constant β. This compares reasonably well with fracture results for UHMWPE of other workers. Ching et al. [5] evaluated a u_e value of 56 kJ/m^2 for UHMWPE, but using a grade different from that measured here. Mai et al. [12] studied two grades of UHMWPE, using both the EWF method and the J-integral approach. The latter method yields a fracture energy value J_c which is equivalent to u_e. The values for u_e were calculated in the range of 77–98 kJ/m^2, while the J_c values were in the range 85–104 kJ/m^2. A further value of J_c for UHMWPE of

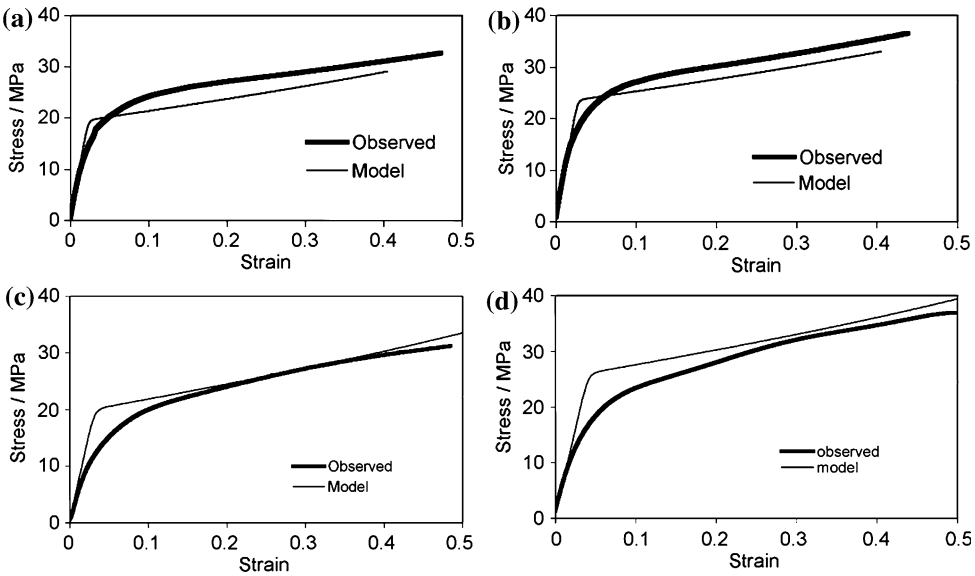

Fig. 6 Comparison of model and observed stress–strain curves in tension at strain rate **a** 0.005 s^{-1} and **b** 0.1 s^{-1}. Comparison of model and observed stress–strain curves in compression at strain rate **c** 0.0005 s^{-1} and **d** 0.017 s^{-1}

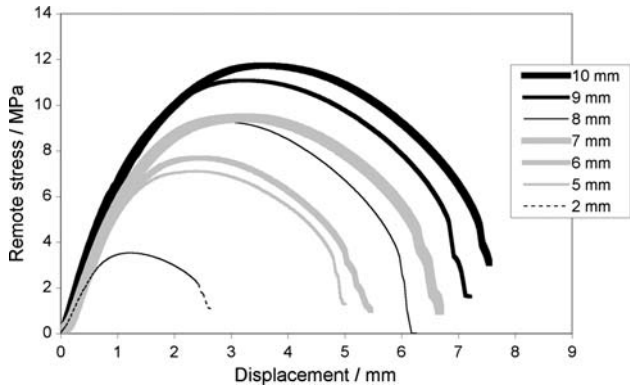

Fig. 7 EWF testing for specimens of thickness 1.5 mm

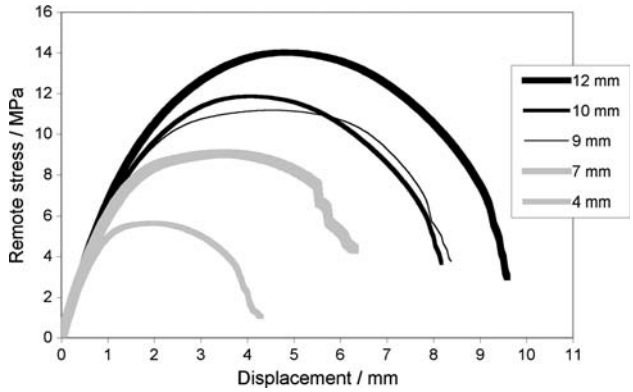

Fig. 8 EWF testing for specimens of thickness 3.0 mm

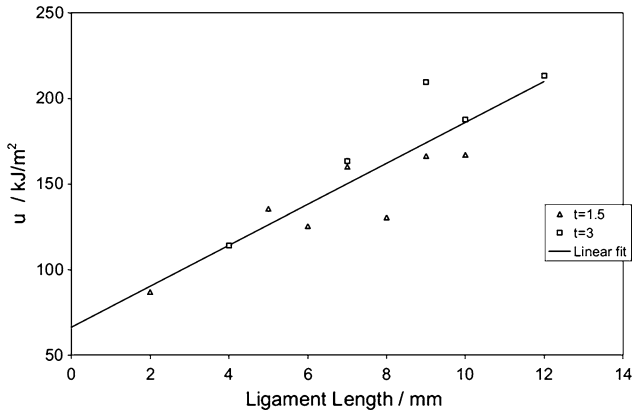

Fig. 9 Specific work plot to give extrapolated value u_e = 66.2 kJ/m^2

99.5 kJ/m^2 has been reported by Rimnac et al. [26]. In summarising the values obtained for J_c for UHMWPE, the review by Pruitt [27] notes that reported values are in the range 66.5–99 kJ/m^2. A specific comparison for the grade of material studied here using the EFW method is provided by Haughie et al. [28], who report a value of u_e of 69 ± 9 kJ/m^2. This is entirely consistent with our estimate.

FE modelling and analysis

The validity of some of the assumptions behind the EWF method will now be explored by modelling. The constitutive equation described above has been implemented within a finite element scheme to model the EWF experiments. The finite element program ABAQUS was used, with the material model implementation via a 'UMAT' user-defined subroutine. The analysis carried out in the subroutine is summarised here. The formulation is similar to that used previously for high temperature stretching of polypropylene [29, 30] in which different elastic network components were used.

At each computed point the deformation is input to the subroutine in the form of the deformation gradient **F**. This strain applies to both arms of the model of Fig. 5.

One arm consists of a network as defined in Eq. 14 in series with an Eyring process (the X arm), and the other entirely of a network of the same kind (the Y arm) defined by Eq. 16. The X and Y arms are associated with stress tensors $\mathbf{\Sigma}^{\mathbf{X}}$ and $\mathbf{\Sigma}^{\mathbf{Y}}$, respectively, defined in global axes. Equations 3 and 4 are now expressed as:

$$\boldsymbol{\tau} = \mathbf{\Sigma}^{\mathbf{X}} - \bar{\sigma}\mathbf{I} \tag{23}$$

and

$$\bar{\sigma} = \frac{1}{3}\mathbf{tr}(\mathbf{\Sigma}^{\mathbf{X}}). \tag{24}$$

The scalar octahedral shear stress τ used in (1) remains as defined in Eq. 5.

There has been a number of approaches to the analysis of elastic–plastic behaviour at large deformation, a useful summary of which has recently been made available by Figiel and Buckley [31]. Following the method that they classify as approach II, we split the deformation gradient **F** multiplicatively into elastic and plastic components in the X arm $\mathbf{F}^{\mathbf{e}}$ and $\mathbf{F}^{\mathbf{p}}$:

$$\mathbf{F} = \mathbf{F}^{\mathbf{e}}\mathbf{F}^{\mathbf{p}}. \tag{25}$$

At this point, the analysis may proceed in a number of ways, depending on how rigid body rotation is distributed between $\mathbf{F}^{\mathbf{e}}$ and $\mathbf{F}^{\mathbf{p}}$. We have assumed that all the rigid body rotation is included in the plastic deformation. This follows the 'approach II, case 2' method as classified by Figiel and Buckley [31]. $\mathbf{F}^{\mathbf{p}}$ is thus split into pure deformation $\mathbf{V}^{\mathbf{p}}$ and rigid body rotation **R** (via the use of the Cauchy–Green strain measure) to give

$$\mathbf{F}^{\mathbf{p}} = \mathbf{V}^{\mathbf{p}}\mathbf{R}. \tag{26}$$

while the elastic deformation gradient is symmetric, with $\mathbf{F}^{\mathbf{e}} = \mathbf{V}^{\mathbf{eX}}$, so that Eq. 25 becomes

$$\mathbf{F} = \mathbf{V}^{\mathbf{eX}}\mathbf{V}^{\mathbf{p}}\mathbf{R}. \tag{27}$$

An incremental approach is used, with strain rate assumed to be constant during each time increment. The current plastic stretch $\mathbf{V}^{\mathbf{p}}$ is related to the plastic strain $\mathbf{V}_{\mathbf{0}}^{\mathbf{p}}$ at the end of the previous time increment and the increment of plastic strain $\Delta\mathbf{V}^{\mathbf{p}}$ developed during the current increment, by

$$\mathbf{F} = \mathbf{V}^{\mathbf{eX}}\Delta\mathbf{V}^{\mathbf{p}}\mathbf{V}_{\mathbf{0}}^{\mathbf{p}}\mathbf{R}. \tag{28}$$

$\mathbf{V}^{\mathbf{eX}}$ and $\Delta\mathbf{V}^{\mathbf{p}}$ are collinear, since the direction of $\Delta\mathbf{V}^{\mathbf{p}}$ is prescribed by the flow rule (6). The magnitudes of the components of $\Delta\mathbf{V}^{\mathbf{p}}$ are such that the components of $\Delta\mathbf{V}^{\mathbf{p}}\mathbf{V}_{\mathbf{0}}^{\mathbf{p}}$ are incremented according to the Eyring equation (1) and the flow rule (6). The values of $\mathbf{V}^{\mathbf{eX}}$ and $\Delta\mathbf{V}^{\mathbf{p}}$ in equation (28) are derived via an iterative process, to impose the condition that the stresses in the network and the Eyring process are equal while the strains in the two elements are related to the total strain by Eq. 28. At each iteration, stresses are generated using Eq. 14 to drive the Eyring process via Eqs. 23, 24 and 1. The values of the plastic and elastic strain components are adjusted until the stresses in the two processes are sufficiently close. The resulting true stress is then transformed to global directions to give the stress tensor $\mathbf{\Sigma}^{\mathbf{X}}$. Finally, the plastic strain tensor $\mathbf{V}^{\mathbf{p}}$ at the end of the time increment is the symmetric part of $\mathbf{F}^{\mathbf{p}}$, with

$$\mathbf{F}^{\mathbf{p}} = \Delta\mathbf{V}^{\mathbf{p}}\mathbf{V}_{\mathbf{0}}^{\mathbf{p}}\mathbf{R} = \mathbf{V}^{\mathbf{p}}\mathbf{R}', \tag{29}$$

where in general the rigid body rotation $\mathbf{R}'$ differs from $\mathbf{R}$. The principal stresses in the Y arm are defined in Eq. 16. When transformed to global directions they yield the stress tensor $\mathbf{\Sigma}^{\mathbf{Y}}$. The total stress $\mathbf{\Sigma}$ is then given by

$$\mathbf{\Sigma} = \mathbf{\Sigma}^{\mathbf{X}} + \mathbf{\Sigma}^{\mathbf{Y}}. \tag{30}$$

As noted by Figiel and Buckley [31], the different possible approaches to the elastic–plastic analysis for arm X will give different numerical results. In their examples, they showed that the stress predictions of the different methods are similar at lower strains, beginning to part company at shear strains of ~ 1 and normal true strains of ~ 1. The maximum strains covered in this study are well below 1, so we conclude that our choice of method should yield an adequate analysis.

Fracture analysis

The above formulation has been implemented in finite element analyses using models of the EWF specimens, one of which is shown in Fig. 10. This is a quarter model of the specimen. A number of models of this type with varying ligament lengths have been run, using material parameters given in Table 1. No attempt was made to model crack propagation. The model specimens were extended by constant speed vertical motion of the upper horizontal boundary while restraining horizontal movement of each node, to mimic the experimental technique. The lower symmetry boundary was constrained in the vertical direction only to allow lateral contraction. A range of notch lengths was used.

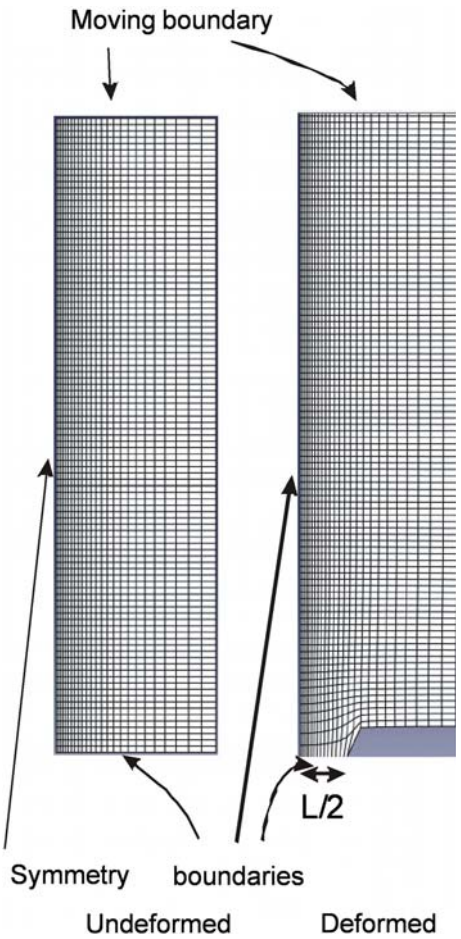

Fig. 10 Mesh for quarter model fracture specimen, for ligament length 9 mm

The use of this analysis allows us to explore the levels of irrecoverable energy expended in extending the model specimen under conditions of no crack propagation—the non-essential work. The energy is calculated from the work done on extending the upper boundary to give the total strain energy W within the quarter model specimen. We assume that cracks grow at a constant crack opening displacement (COD), as supported by our video capture the experiments. We shall present results calculated for a series of ligament lengths for specimens stretched to give the same value of COD, by a vertical displacement u_{COD} which depends on the ligament length. Thus,

$$w = \int_0^{u_{\mathrm{COD}}} F\,\mathrm{d}u \tag{31}$$

gives the total energy w when the finite element model is used with the material model defined above and specified

by the parameters of Table 1. Lower-case letters are used here for energies associated with the non-growing cracks of the FE models. To calculate the plastic energy corresponding to the non-essential work, we subtract from w the elastic strain energy in the model specimen w_{elas}. The latter is calculated using the same meshes and material model as for calculating w, but with the Eyring process inactive; the material parameters are as in Table 1 except that the activation volume parameters V_s and V_p are so small that the strain in the Eyring process is negligible. The elastic models are extended such that the maximum boundary force $F_{\max}$ is the same as that attained in the calculation of w in Eq. 31, to an extension that we denote by u_{fmax}. While we require the elastic energy to be calculated over the whole of the specimen outside the yielded zone, this procedure also includes the elastic energy in the volume of material that becomes the plastic zone. However, since the volume of the plastic zone is typically <2% of the volume of the specimen, we consider this to cause an insignificant error. Thus, to a good approximation,

$$w_{\text{elas}} = \int_0^{u_{\text{fmax}}} F_{\text{elas}}\, \mathrm{d}v, \tag{32}$$

where $F_{\max}$ is the boundary force calculated using the elastic model. The non-essential work is now given by

$$w_{\text{ne}} = w - w_{\text{elas}}. \tag{33}$$

We have chosen a numerical value of COD of 1.7 mm and related this to the vertical displacement of the node adjacent to that at the notch tip, so that V_{COD} corresponds to the displacement of the node of 0.85 mm. This value of COD is realistic according to the video observations of the fracture experiments, though we would expect similar conclusions from the foregoing analysis for arbitrary COD values. Numerical evaluation of the integrals in Eqs. 31 and 32 have been used to derive values of W_{ne} for a range of ligament lengths.

In Fig. 11, we plot the results of simulations carried out at a rate of deformation corresponding to the experimental speed of 10 mm/min. It is clear that w_{ne} is a linear function of ligament length to a very good approximation. There are grounds for expecting a zero intercept in Fig. 11, whereas the intercept is clearly positive. In the arguments for the EWF method outlined above, it is assumed that the non-essential work is proportional to the volume of the plastic zone. This would lead to a zero intercept to correspond to the implied zero volume of yielded material. The assumption is justified for simple elastic–plastic behaviour, but in the constitutive model used here the material is time-dependent; the energy within yielded material dissipates with time. For higher ligament lengths, the fixed COD is reached after longer times, with a corresponding increased tendency for w_{ne} to decay. This will lead to a tendency to a positive intercept. To explore the importance of this effect, we have conducted a set of simulations that correspond to a higher testing speed of 20 mm/min, for which we would expect the tendency for a positive intercept to be less. The results, also plotted in Fig. 11, show a smaller positive intercept.

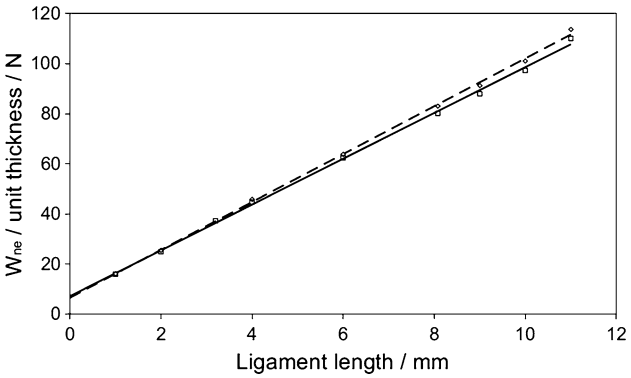

Fig. 11 Non-essential work as calculated from FE models, for testing speeds 10 mm/min (◇) and 20 mm/min (□). The intercept for the higher speed is 9% lower than for the lower speed

If we accept that under certain ideal conditions, the intercepts in plots like those in Fig. 11 would be zero, or that in any case we may use the zero intercept as a reasonable approximation, we have

$$w_{\text{ne}} = \alpha \ell t \tag{34}$$

for a gradient α and ligament half-length ℓ. Suppose that at any crack length there is a plastic zone extending to a distance r normal to the crack. Then, the plastic zone has a volume v

$$v = \gamma r^2 t, \tag{35}$$

where γ is a shape factor in the same spirit as β in Eq. 21, but applying as a local value for the growing crack rather than for the complete grown crack. Suppose further, in common with the conventional analysis, that the volume of the plastic zone is proportional to the non-essential work. Then,

$$w_{\text{ne}} = \eta r^2 t, \tag{36}$$

where η is simply related to γ. Equating (21) and (21) now gives

$$r = \sqrt{\frac{\alpha \ell}{\eta}}. \tag{37}$$

Suppose that a crack extends from an initial ligament length L to complete fracture. Then, the total volume of the plastic zone after passage of the crack V is given by

$$V = 2t \int_0^{L/2} r \, \mathrm{d}\ell, \tag{38}$$

which by the use of Eq. 37 becomes

$$V = 2t \int_0^{L/2} \sqrt{\frac{\alpha\ell}{\eta}} \, \mathrm{d}\ell. \tag{39}$$

This can be integrated to give a simple expression provided that η is independent of ℓ. However, in general this assumption will not be correct. It can be envisaged that, as the crack depth increases, the yielded region ahead of it will begin to confront the symmetry boundary, so that its forward extent will become a lower proportion of its normal extent r, so that η will decrease. However, a constant η could be maintained for a good proportion of the integral for the case of small plastic zones. To examine this limiting case, we integrate Eq. 39 at constant η to give

$$V = \frac{\sqrt{2}t}{3}\sqrt{\frac{\alpha}{\eta}}L^{3/2}. \tag{40}$$

We now equate this volume with that occurring in Eq. 21 ($V = \beta L^2 t$) to give for the shape factor β

$$\beta = \frac{1}{3}\sqrt{\frac{\alpha}{2\eta}}L^{-1/2}. \tag{41}$$

The dependence of β on L apparent from Eq. 41 is in direct contradiction to the constancy of β assumed in the conventional analysis. The use of this expression for β in the original equation (22) gives the result:

$$u = u_e + u_{ne}AL^{1/2} \tag{42}$$

This resembles the relation proposed by Levita et al. [25]:

$$u = B + CL^n. \tag{43}$$

They found that optimised fits to their data invariably produced very low, effectively zero, values of B, with exponent n in the range 0.56–0.72. The power law (43) with $B = 0$ represented their data for polymer films very well, but was clearly not useful for deriving u_e. Similarly, we have found that optimised fits of Eq. 42 to our data give $u_e = 0$. In the theory above Eq. 42 is associated with a function β of Eq. 41 that is singular at $L = 0$, and a similar observation can apply to Eq. 43 if it is interpreted in terms of a similar theory for $0 < n < 1$; the poor extrapolating behaviour towards $L = 0$ can be interpreted in terms of a singularity in β.

We now explore the validity of one of the major assumptions behind the EWF method by examining the finite element results. This assumption is that the energy density u_{ne} is constant. There are no a priori physical grounds for this assumption. Even for simple elastic–plastic behaviour with a constant yield stress, once an element of material has been taken to its yield stress, it can be extended further to an arbitrary extent at constant stress while an arbitrary amount of work is done on it. Under the conditions of fracture of the EWF method, it may be expected that the extension applied to the plastic zone is limited as it will cease once the crack has passed, so there will be some natural limit to u_{ne}. To quantify this, we compare the non-essential work deduced so far from the boundary extensions with the volumes of yielded material predicted by the models. We derive contour plots that approximate to the plastic zones by assuming a von Mises yield stress of 25 MPa, consistent with our stress–strain observations at higher strain rates. In Fig. 12, we show contour plots of von Mises stress for various ligament lengths L at a constant COD of 1.7 mm. These are plotted on the undeformed model so that the thickness remains constant and the areas can be simply related to volumes, bearing in mind that the theory is for incompressible material. These plastic zones relate to non-propagating notches; the plastic zones of concern in the EWF method are those associated with a crack that has completely propagated through the specimen. In the case where the ligament has fully yielded before crack propagation, there

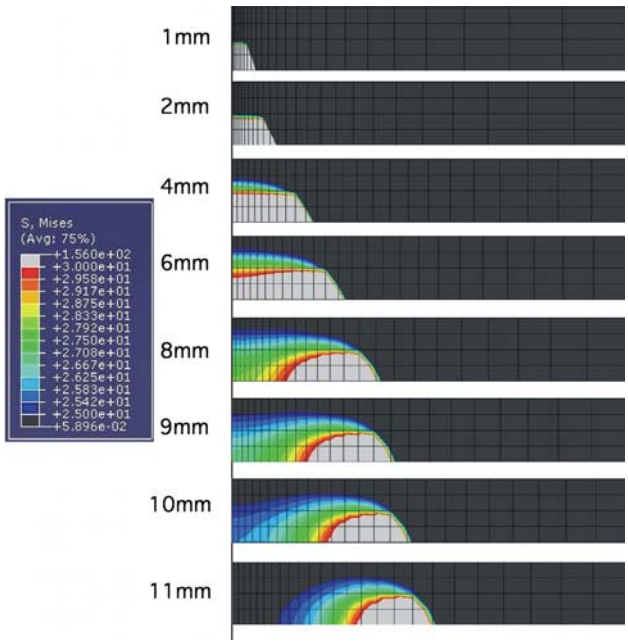

Fig. 12 Contour plots of von Mises stress for different ligament lengths showing the extent of the plastic zones. The plots are for the full width of the models (e.g. Fig. 11) for the region above the lower symmetry boundary

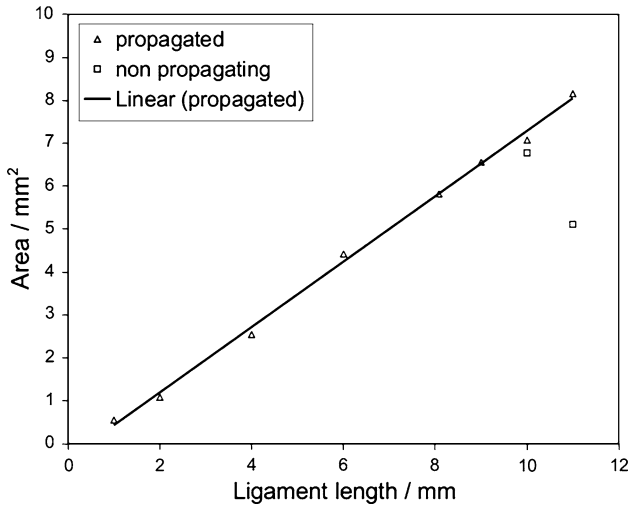

Fig. 13 Areas (=volume/unit thickness) of plastic zones from FE analyses. Results for non-propagating cracks are plotted only when different from those for propagated cracks

is little difference in the extent of these zones. For values of ligament of 9 mm or less, the model zone is larger than for smaller ligaments, and so a good estimate is simply that the model zone is equal in size to that for the fully propagated crack. For ligament lengths of 10 and 11 mm, this is not the case and we estimate the final zone area by assuming that the model zone propagates at constant height. In this way, we can use the finite element results to derive the volumes of both types of plastic zone. These are plotted in Fig. 13. For the zones associated with the propagated cracks, there is a linear relationship with ligament length. When associated with the non-essential work plotted in Fig. 11 and the associated equation (34), the clear implication is that u_{ne} is constant to a good approximation. Comparing the slopes of the two figures gives a value $u_{ne} = 12.5$ J mm^{-3}. For the zones associated with non-propagated cracks u_{ne} is increased at the higher ligament lengths.

From Fig. 12 it is clear that, as L increases, the zone elongates so that β is clearly dependent on L. We have calculated β using the area measurements discussed above, and the result as plotted in Fig. 14 shows that it varies considerably with ligament length. To examine the implications of this variation for the extrapolated u_e value, we have plotted u against βL in Fig. 15; according to equation, this should give a linear relationship. In this plot, we have used the calculated values of β of Fig. 14, smoothed using a power law function to avoid introducing noise into the plot. The extrapolated value for u_e is little changed from the original plot of Fig. 9; the value is now 65.4 ± 38 rather than 66 ± 15 kJ m^{-2}. However, the error in the intercept has been greatly increased, reflecting the smaller range in the x-values. In this case, there is seemingly no advantage in the use of the calculated β values.

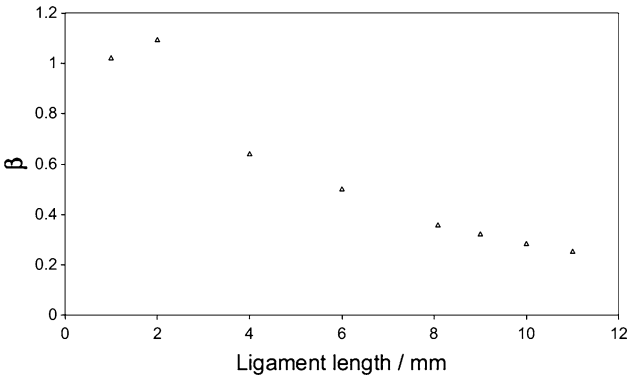

Fig. 14 β calculated from FE analyses

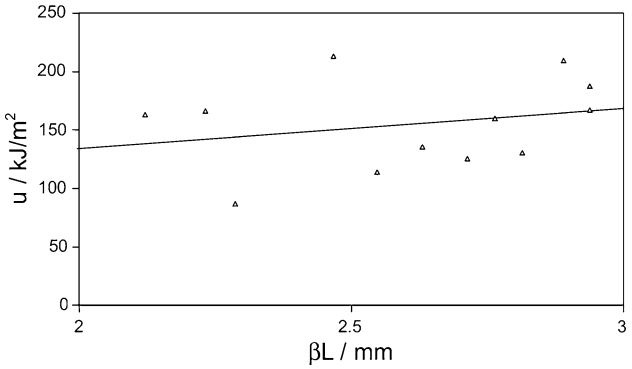

Fig. 15 Specific work plot as a function of $\beta \times$ ligament length to give extrapolated value u_e = 65.4 kJ/m^2

Conclusions

For the purpose of examining the validity of the EWF method of fracture testing when applied to UHMWPE, we have developed a constitutive model that provides a good overall description of the behaviour of UHMWPE in both uniaxial tension and compression. In particular, the strain rate dependence of stress, including the small difference between tension and compression, is modelled via an Eyring process. This model has been incorporated via a user-defined subroutine into the commercial finite element package ABAQUS.

We have carried out a programme of double-edge notch tensile testing of UHMWPE specimens. The results have been analysed using the method conventionally employed with EWF, and fracture energy values derived similar to those obtained by other workers. The EWF specimens have been modelled using the finite element implementation of the constitutive model. This has allowed some basic assumptions of the conventional EWF analysis to be addressed, namely the constancy of the non-essential work and the constancy of the plastic zone shape factor. By using an energetic analysis of the finite element model results,

and also evaluating plastic zone sizes, it is concluded that the specific non-essential work u_{ne} is constant to a good approximation. The shape factor β, assumed constant in the conventional EWF analysis, is shown to vary strongly with ligament length. The implications of this on the calculated values of the EWF are examined, and for the experiments discussed here they are found not to be significant. The calculated value of u_e is found to be 66 $\pm$ 15 kJ m^{-2}.

Acknowledgements We wish to thank Dr. Neil Hubbard, Orthoplastics, Todmorden Road, Bacup, Lancs, UK for supply of material. We acknowledge funding from EPSRC for Dr. Naz under the Doctoral Training scheme.

References

1. Bergström JS, Kurtz SM, Rimnac CM, Edidin AA (2002) Biomaterials 23:2329
2. Bergström JS, Rimnac CM, Kurtz SM (2003) Biomaterials 24:1365
3. Bergström JS, Rimnac CM, Kurtz SM (2004) Biomaterials 25:2171
4. Kurtz SM, Muratoglu OK, Evans M, Edidin AA (1999) Biomaterials 20:1659
5. Ching ECY, Poon WKY, Li RKY, Mai Y-W (2000) Polym Eng Sci 40:2558
6. Yamakawa RS, Razzino CA, Correa CA, Hage E Jr (2004) Polym Test 23:195
7. Hashemi S (2003) Polym Test 22:589
8. Poon WKY, Ching ECY, Cheng CY, Li RKY (2001) Polym Test 20:395
9. Karger-Krocsis J, Moskala EJ (2000) Polymer 41:6301
10. Mai YW, Cotterell B (1986) Int J Fracture 30:R37
11. Broberg KB (1968) Int J Fracture 4:11
12. Mai YW, Cotterell B, Horlyck, Vigna G (1987) Polym Eng Sci 27:804
13. Hart EW (1967) Acta Metall 15:351
14. Coates PD, Ward IM (1980) J Mater Sci 15:2897. doi:10.1007/BF00550561
15. Sweeney J, Shirataki H, Unwin AP, Ward IM (1999) J Appl Polym Sci 74:3331
16. Ward IM, Sweeney J (2004) An introduction to the mechanical properties of solid polymers. Wiley, Chichester
17. Chow TS (1992) J Rheol 38:1707
18. Haward RN, Thackray G (1968) Proc Roy Soc A 302:453
19. Nazarenko S, Bensason S, Hiltner A, Baer E (1994) Polymer 35:3883
20. Bauwens-Crowet C, Bauwens J-C, Homès G (1972) J Mater Sci 7:176. doi:10.1007/BF02403504
21. Joseph SH, Duckett RA (1978) Polymer 19:837
22. Truss RW, Duckett RA, Ward IM (1981) J Mater Sci 16:1689. doi:10.1007/BF02396889
23. Brooks NWJ, Duckett RA, Ward IM (1995) J Rheol 39:425
24. Gueguen O, Richeton J, Ahzi S, Makradi A (2008) Acta Mater 56:1650
25. Levita G, Parisi L, Mcloughlin S (1996) J Mater Sci 31:1545. doi:10.1007/BF00357863
26. Rimnac CM, Wright TM, Klein RW (1988) Polym Eng Sci 28:1586
27. Pruitt LA (2005) Biomaterials 26:905
28. Haughie DW, Buckley CP, Wu J (2006) Biomaterials 27:3875
29. Spencer PE, Sweeney J, Coates PD (2008) Mech Time-Dependent Mater 12:313
30. Sweeney J, Spares R, Woodhead M (2009) Polym Eng Sci 49:1902
31. Figiel L, Buckley CP (2009) J Non-Linear Mech 44:389